Coherent and incoherent phase stabilities of thermoelectric rocksalt IV-VI semiconductor alloys

Jeff W. Doak and C. Wolverton

Department of Materials Science and Engineering, Northwestern University, Evanston, Illinois, USA 60208

(Received 27 June 2012; revised manuscript received 26 September 2012; published 15 October 2012)

Nanostructures formed by phase separation improve the thermoelectric figure of merit in lead chalcogenide semiconductor alloys, with coherent nanostructures giving larger improvements than incoherent nanostructures. However, large coherency strains in these alloys drastically alter the thermodynamics of phase stability. Incoherent phase stability can be easily inferred from an equilibrium phase diagram, but *coherent* phase stability is more difficult to assess experimentally. Therefore, we use density functional theory calculations to investigate the coherent and incoherent phase stability of the IV–VI rocksalt semiconductor alloy systems Pb(S,Te), Pb(Te,Se), Pb(Se,S), (Pb,Sn)Te, (Sn,Ge)Te, and (Ge,Pb)Te. Here we use the term coherent to indicate that there is a common and unbroken lattice between the phases under consideration, and we use the term incoherent to indicate that the lattices of coexisting phases are unconstrained and allowed to take on equilibrium volumes. We find that the thermodynamic ground state of all of the IV–VI pseudobinary systems studied is incoherent phase separation. We also find that the coherency strain energy, previously neglected in studies of these IV–VI alloys, is lowest along [111] (in contrast to most fcc metals) and is a large fraction of the thermodynamic driving force for incoherent phase separation in all systems. The driving force for coherent phase separation is significantly reduced, and we find that coherent nanostructures can only form at low temperatures where kinetics may prohibit their precipitation. Furthermore, by calculating the energies of ordered structures for these systems we find that the coherent phase stability of most IV–VI systems favors ordering over spinodal decomposition. Our results suggest that experimental reports of spinodal decomposition in the IV–VI rocksalt alloys should be re-examined.

DOI: 10.1103/PhysRevB.86.144202 PACS number(s): 64.75.Nx, 64.70.kg, 82.60.Nh, 84.60.Rb

I. INTRODUCTION

Chalcogenide semiconductors and semiconductor alloy systems form a class of promising thermoelectric materials with high figures of merit ($ZT = \frac{S^2\sigma}{\kappa}$).[1–12] The prototypical example is PbTe, with a ZT approaching 1.0.[13] It has recently been shown that alloying PbTe with other semiconductor systems can increase the figure of merit through the formation of nanoscale precipitates, which reduce the lattice thermal conductivity, κ, of the system without significantly reducing the electronic conductivity, σ.[7,11] This lack of carrier scattering has been attributed to coherent interfaces between PbS-rich precipitates and the PbTe-rich matrix.[7,14] A coherent interface between two phases maintains a common (possibly strained) lattice between the phases which is not broken by misfit dislocations. Optimizing the effects of nanostructures on thermoelectric transport properties in a bulk material requires understanding and controlling the mechanisms by which nanoscale precipitates form.

The PbS precipitates seen in Pb(S,Te) are a consequence of the chemical thermodynamics of mixing in this system. The temperature–composition phase diagram of Pb(S,Te) contains a miscibility gap:[15–18] a region where PbS and PbTe are not soluble in one another, and a PbS-rich phase may precipitate out of a PbTe-rich supersaturated solid solution. Within a miscibility gap, the solid solution can either be unstable or metastable with respect to phase separation; the boundary between these two regions is called the spinodal line. Outside of the spinodal, the solid solution is metastable, and phase separation proceeds by a nucleation and growth mechanism. Inside the spinodal, the solid solution is unstable, and phase separation occurs by spinodal decomposition. A schematic miscibility gap is plotted in Fig. 1.

The spinodal line itself is difficult to measure experimentally, and so it is often approximated by the chemical spinodal, which is given by the locus of points satisfying $\frac{d^2G_m}{dx^2} = 0$, where G_m is the free energy of mixing (fit to the miscibility gap). While this chemical spinodal is applicable to immiscible fluids, it ignores the (often large) effects of strain due to lattice mismatch in a solid solution.[19] The chemical spinodal is shown as a dotted (red) line in Fig. 1. The chemical spinodal always touches the incoherent miscibility gap at a temperature, T_c, called the critical temperature. As will be subsequently shown, this does not need to be the case when the effects of strain are taken into account.

In addition to the equilibrium phase diagram, governed by incoherent phase separation, coherency strains caused by large lattice mismatches can lead to another metastable, coherent phase diagram. Spinodal decomposition is, by definition, a coherent decomposition pathway and thus is dictated by this metastable coherent phase stability. Pb(S,Te) is such a system with a large lattice mismatch between the constituent compounds ($a_{\mathrm{PbS}} = 5.936$ Å, $a_{\mathrm{PbTe}} = 6.454$ Å, ~8% lattice mismatch[20]), and so it is the *coherent* spinodal which separates the regions of different phase separation mechanisms.[19,21,22] Here we use the term coherent to indicate that there is a common and unbroken lattice (say, by misfit dislocations) between the phases under consideration. The coherent spinodal can be found by explicitly incorporating an elastic strain energy term into the equation for the chemical spinodal,[21]

$$\frac{\partial^2 G_m}{\partial x^2} + 2\eta^2 Y = 0, \tag{1}$$

where η is the linear expansion per unit composition change, and Y is the appropriate effective modulus ($\frac{E}{[1-\nu]}$ in the isotropic case and a linear combination of elastic constants

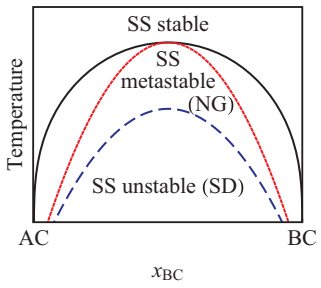

FIG. 1. (Color online) Schematic phase diagram of a pseudobinary (A,B)C alloy system containing a miscibility gap (solid black line). Outside the miscibility gap the solid solution (SS) is stable and inside the gap phase separation occurs. The coherent spinodal (blue dashed line) divides the miscibility gap into two regions. Outside the coherent spinodal, the solid solution is metastable with respect to phase separation, and phase separation proceeds by nucleation and growth (NG). Inside the coherent spinodal the solid solution is unstable with respect to phase separation, and phase separation proceeds by spinodal decomposition (SD). The unphysical chemical spinodal is also plotted for comparison (red dotted line).

in the anisotropic case). Thus, in any phase separating system with elastic strain, the spinodal will be depressed from the miscibility gap. The coherent spinodal is shown in Fig. 1 as a dashed (blue) line.

The coherent spinodal is particularly difficult to determine experimentally, as coherent phase separation is metastable with respect to incoherent phase separation, and, given enough time, any coherently phase-separated microstructure will coarsen into an incoherent phase separated microstructure. Likewise, there is no way to obtain the coherent spinodal purely from the measured equilibrium phase diagram. So, what is needed is an accurate and predictive method to calculate the coherent spinodal. First-principles calculations are ideally suited to study coherent phase stability in the IV–VI rocksalt alloys. Density functional theory (DFT) calculations have been applied to phase stability problems in metallic alloys,[23–33] semiconductor alloys,[34–41] and oxide systems[42–47] with great success. Lead chalcogenide compounds and alloys have also been studied extensively with DFT, focusing mostly on either the electronic structure[48–62] or lattice dynamics[41,63–69] of these materials. In addition, several studies have looked at the phase stability of these systems, calculating incoherent miscibility gaps and chemical spinodals,[61,62] as well as investigating the relative energetics of ordered and disordered alloys.[50] However, to the best of the authors' knowledge, the effects of coherency strain on the phase stability of IV–VI alloys have not been investigated.

In this study, the coherent phase stability of a series of IV–VI rocksalt semiconductor alloys are systematically investigated through first-principles DFT calculations. Six pseudobinary alloy systems are explored: Pb(S,Te), Pb(Te,Se), Pb(Se,S), (Pb,Sn)Te, (Sn,Ge)Te, and (Ge,Pb)Te. There have been numerous experimental studies of the equilibrium phase stability of these systems.[15–18,70–80] The first three systems mix on the anion sublattice of rocksalt, and the last three mix on the rocksalt cation sublattice. The model of coherent phase stability used here consists of three parts. (i) Mixing enthalpies of the rocksalt solid solution are found through total energy calculations of special quasirandom structures (SQS).[81,82] (ii) The Gibbs free energy of mixing is obtained by adding an ideal entropy term to the enthalpy of mixing. (iii) Finally, coherency strain energy calculations provide the energies of coherent phase separation. From these first-principles energetic quantities, we extract the incoherent and coherent Gibbs free energies (in the form of subregular solution models), and we calculate the incoherent miscibility gaps and coherent spinodals for each system.

From our first-principles calculations, we find that the mixing enthalpies of all IV–VI systems studied are positive, consistent with the phase separation experimentally observed in most of these systems. In addition, we find that the coherency strain energy is lowest along the [111] direction and highest along the [100] direction for all of the systems investigated. This strain anisotropy is contrary to many (fcc) metallic systems, where the [100] and [111] directions are often the elastically softest and hardest directions, respectively. Furthermore, we find that the coherency strain energy is a significant fraction of the enthalpy of mixing, indicating that most of the energy required to mix the constituents of these systems goes towards straining the constituents onto the same lattice, and that the coherency strain energy cannot simply be neglected in any analysis of coherent phase stability of these systems. Indeed, when the systems are constrained to phase separate coherently, we find that the coherent spinodal is depressed significantly in temperature from both the chemical spinodal and the incoherent miscibility gap. This depression is large enough that spinodal decomposition can only occur at very low temperatures, where it will likely be kinetically unfeasible. In addition, we find that the incoherent miscibility gap temperatures in these systems scale with the coherency strain energy of the system, further evidence that the main driving force for phase separation in the IV–VI rocksalt semiconductor alloys is lattice mismatch strain.

II. FREE ENERGY MODEL

We begin with a description of the various terms in our model for the free energy of mixing. We can define two different Gibbs free energies of mixing, an incoherent free energy of mixing, $\Delta G^{\text{incoh}}_{\text{mix}}(x,T)$, and a coherent free energy of mixing, $\Delta G^{\text{coh}}_{\text{mix}}(x,T)$, which describe the free energies of the solid solution with respect to incoherent and coherent phase separation, respectively. Both free energies of mixing are functions of composition, x, and temperature, T. These free energies can be expressed in terms of the incoherent, $\Delta H^{\text{incoh}}_{\text{mix}}(x)$, and coherent, $\Delta H^{\text{coh}}_{\text{mix}}(x)$, enthalpies of mixing, as well as the ideal entropy of mixing or ideal configurational entropy, $\Delta S^{\text{ideal}}_{\text{mix}}(x)$, as,

$$\begin{aligned}\Delta G^{\text{incoh}}_{\text{mix}}(x,T) &= \Delta H^{\text{incoh}}_{\text{mix}}(x) - T\Delta S^{\text{ideal}}_{\text{mix}}(x),\\ \Delta G^{\text{coh}}_{\text{mix}}(x,T) &= \Delta H^{\text{coh}}_{\text{mix}}(x) - T\Delta S^{\text{ideal}}_{\text{mix}}(x).\end{aligned} \tag{2}$$

The ideal mixing entropy is given by

$$\Delta S^{\text{ideal}}_{\text{mix}}(x) = -k_B\left[x\ln x + (1-x)\ln(1-x)\right]. \tag{3}$$

The incoherent and coherent enthalpies of mixing describe the enthalpies of the solid solution with respect to incoherent and coherent phase separation, respectively. The incoherent

enthalpy of mixing is given by

$$\Delta H_{\text{mix}}^{\text{incoh}}(x) = E_{\text{random}}(x) - (1-x)E_{AC} - xE_{BC}, \quad (4)$$

where E_{random} is the energy of the solid solution, and E_{AC} and E_{BC} are the energies of the constituent compounds. The difference between the incoherent and coherent enthalpies of mixing is the difference in energy between the coherent and incoherent reference states. Thus, we can relate the coherent enthalpy of mixing to the incoherent enthalpy of mixing by

$$\Delta H_{\text{mix}}^{\text{coh}}(x) = \Delta H_{\text{mix}}^{\text{incoh}}(x) - \Delta E_{CS}^{\text{min}}(x), \quad (5)$$

where $\Delta E_{CS}^{\text{min}}(x)$ is the minimum coherency strain energy, the lowest energy possible for a system in a phase separated state with both phases completely coherent with one another. In the next sections we will describe how each of the terms in Eqs. (2)–(5) will be calculated within DFT.

A. Incoherent enthalpies of mixing, $\Delta H_{\text{mix}}^{\text{incoh}}(x)$

Enthalpies of mixing of the random or disordered solid solution are difficult to compute directly from DFT, since these methods are typically used to compute properties of ordered periodic arrangements of atoms. To overcome this difficulty, we use the method of SQS.[81,82] These SQSs are small unit cell (32 atoms in this study) ordered structures, with atoms placed on lattice sites in such a way as to mimic the pair and multibody correlations of a perfectly random lattice. This methodology allows for the accurate, DFT-level treatment of random solid solutions, including the important physical effects of local atomic relaxations, without the computational cost of a large supercell, where A and B atoms are randomly arranged on the lattice sites. Since mixing only occurs on one fcc sublattice of the rocksalt lattice in any of the pseudobinary systems considered here, previously generated fcc SQSs[30] will be modified by adding atoms to the fcc octahedral sites, creating rocksalt SQSs with mixing on only one fcc sublattice. Two SQS supercells will be used, one with a composition of $A_{0.5}B_{0.5}C$ (e.g., $Pb_{0.5}Ge_{0.5}Te$ and $PbS_{0.5}Te_{0.5}$ for cation and anion mixing, respectively) and the other of $A_{0.25}B_{0.75}C$. By switching the A and B atoms in the second case, a stoichiometry of $A_{0.75}B_{0.25}C$ can be obtained.

To model the thermodynamics of solid-solid mixing in these systems, a subregular solution model,

$$\Delta H_{\text{mix}}^{\text{incoh}}(x) = \alpha_{\text{incoh}}x(1-x) + \beta_{\text{incoh}}x(1-x)(1-2x), \quad (6)$$

is fit to the formation energies of the three SQSs from each pseudobinary system with fitting parameters α_{incoh} and β_{incoh} (Table I contains these parameters for each pseudobinary system considered). To model mixing with respect to incoherent phase separation, the reference state for this enthalpy is the energy of incoherent phase separation, i.e.,

$$E_{\text{IPS}}(x) = (1-x)E_{AC} + xE_{BC}, \quad (7)$$

where E_{AC} and E_{BC} are the total energies of bulk rocksalt pseudobinary constituents [e.g., PbS and PbTe in Pb(S,Te)], each relaxed to their equilibrium bulk lattice parameters, and x is the mole fraction of BC in the system.

TABLE I. Subregular solution model mixing enthalpy fitting parameters for each pseudobinary system. Fitting parameters for both the incoherent and coherent mixing enthalpies are provided [Eqs. (5) and (10), respectively].

	α_{incoh} (meV/cat)	β_{incoh} (meV/cat)	α_{coh} (meV/cat)	β_{coh} (meV/cat)
$PbS_{1-x}Te_x$	289.5	47.07	74.62	41.79
$PbTe_{1-x}Se_x$	107.4	−8.43	27.47	−6.06
$PbSe_{1-x}S_x$	47.36	−2.21	14.70	−2.03
$Pb_{1-x}Sn_xTe$	25.66	−0.23	10.18	−0.18
$Sn_{1-x}Ge_xTe$	105.4	−11.80	−6.77	−23.88
$Ge_{1-x}Pb_xTe$	173.5	−57.62	−39.77	−52.59

B. Coherency strain energies, $\Delta E_{CS}^{\text{min}}(x)$

To model the coherent enthalpy of mixing, the reference state must be changed from incoherent phase separation to coherent phase separation via Eq. (5). This change in reference state is accomplished by adding the minimum coherency strain energy to the energy of incoherent phase separation, or equivalently, subtracting the minimum coherency strain energy from the incoherent enthalpy of mixing. The coherency strain energy is the energy required to strain two phases onto the same lattice parameter along a crystallographic direction (with the minimum coherency strain energy occurring along the elastically softest direction). The coherency strain energy, $\Delta E_{CS}(\hat{k},x)$ depends on both the direction, $\hat{k}$, along which the phases are strained and the amount of each phase present, x. A method for calculating the coherency strain energy is given below, following Refs. 27 and 83.

The energy required to strain a phase i to a lattice parameter $a_\perp$ in the plane normal to $\hat{k}$ while allowing the lattice parameter $a_\parallel$ along $\hat{k}$ to relax is defined as the epitaxial strain energy, given by

$$\Delta E_i^{\text{epi}}(\hat{k},a_\perp) = \min_{a_\parallel}[E_i(\hat{k},a_\perp,a_\parallel) - E_i(a_0)], \quad (8)$$

where $E_i(a_0)$ is the energy of phase i at its equilibrium lattice parameter, and $E_i(\hat{k},a_\perp,a_\parallel)$ is the energy of phase i strained to a lattice parameter of $a_\parallel$ along a direction $\hat{k}$, and a lattice parameter of $a_\perp$ in the plane normal to the direction $\hat{k}$. The coherency strain energy of an alloy system can be obtained from the epitaxial strain energies of the constituents (AC and BC) by straining both AC and BC to the same lattice parameter $a_\perp$ normal to $\hat{k}$, and minimizing the total strain energy of the system with respect to this lattice parameter,

$$\Delta E_{CS}(\hat{k},x) = \min_{a_\perp}\left[(1-x)\Delta E_{AC}^{\text{epi}}(\hat{k},a_\perp) + x\Delta E_{BC}^{\text{epi}}(\hat{k},a_\perp)\right]. \quad (9)$$

The minimum coherency strain energy is then the coherency strain energy along the elastically softest direction,

$$\Delta E_{CS}^{\text{min}}(x) = \min_{\hat{k}} \Delta E_{CS}(\hat{k},x). \quad (10)$$

The epitaxial strain energies in Eq. (7) can be obtained from DFT static calculations at the specified lattice parameters. The automated calculation of coherency strain energies for cubic crystals can be performed using the Alloy Theoretic Automated Toolkit (ATAT).[84] By fitting the right-hand side

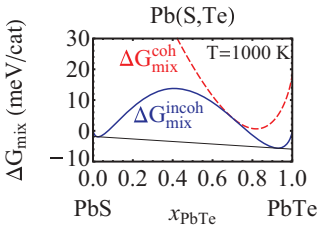

FIG. 2. (Color online) Illustration of the incoherent (blue solid line) and coherent (red dashed line) Gibbs free energies of mixing (2) for the system Pb(S,Te) as a function of mole fraction PbTe at T = 1000 K. The common tangent rule (solid black line) shows the equilibrium concentrations of PbTe in the PbS- and PbTe-rich incoherent phases. The intercepts of the tangent line with the $x_{PbTe} = 0$ and 1 give the chemical potentials of PbS and PbTe, respectively. At 1000 K, the coherent phase diagram exhibits complete solid solubility, while the incoherent phase diagram contains a two-phase miscibility gap. For illustrative purposes, the incoherent and coherent free energies of mixing were made to coincide at a composition of 0.7 mole fraction PbTe.

of Eq. (5) to a subregular solution model form, we obtain an analytical function for the coherent enthalpy of mixing,

$$\Delta H_{mix}^{coh}(x) = \alpha_{coh} x(1-x) + \beta_{coh} x(1-x)(1-2x), \quad (11)$$

where the α_{coh} and β_{coh} are fitting parameters, given in Table I for each IV–VI rocksalt pseudobinary system. A comparison of the coherent enthalpy of mixing model presented here with previous work is provided in the Appendix.

C. Phase diagram calculations

The incoherent and coherent Gibbs free energies of mixing for the system Pb(S,Te) (calculated as described in Sec. IV) are illustrated in Fig. 2 for a temperature below the incoherent miscibility gap but above the coherent miscibility gap. At this temperature, the incoherent free energy of mixing has two minima corresponding to the PbS- and PbTe-rich phases, while the coherent free energy of mixing has only one minima, corresponding to a solid-solution of PbS and PbTe. Equilibrium between the two incoherent phases is found by setting the chemical potentials of each compound (AC and BC) in each phase (α and β) equal to each other,

$$\mu_{AC}^{\alpha} = \mu_{AC}^{\beta}, \quad \mu_{BC}^{\alpha} = \mu_{BC}^{\beta}. \quad (12)$$

This procedure is illustrated graphically in Fig. 2 as the common-tangent rule. The chemical potentials of the binary compounds can be found from the Gibbs free energy (coherent or incoherent) via

$$\mu_{AC}(x) = \Delta G_{mix}(x) - x\frac{\partial \Delta G_{mix}}{\partial x},$$
$$\mu_{BC}(x) = \Delta G_{mix}(x) + (1-x)\frac{\partial \Delta G_{mix}}{\partial x}. \quad (13)$$

In addition to the miscibility gap, the coherent spinodal line can be calculated by taking the second derivative of the coherent Gibbs free energy and setting it to zero, which, for the subregular solution model has the form,

$$\frac{\partial^2 \Delta G_{mix}^{coh}}{\partial x^2} = k_B T\left(\frac{1}{x} + \frac{1}{1-x}\right) - 2\alpha_{coh} - 6\beta_{coh}(1-2x), \quad (14)$$

and the resulting coherent spinodal temperature can be written as a function of composition as

$$k_B T_{sp}(x) = 2\alpha_{coh} x(1-x) + 6\beta_{coh} x(1-x)(1-2x). \quad (15)$$

By utilizing these procedures, incoherent miscibility gaps and coherent spinodals are constructed for each of the six pseudobinary systems considered.

III. COMPUTATIONAL METHODOLOGY

DFT[85,86] calculations were performed using the Vienna *Ab initio* Simulation Package (VASP)[87] with projector augmented wave (PAW)[88] pseudopotentials utilizing the generalized gradient approximation (GGA) and exchange-correlation functional of Perdew, Burke, and Ernzerhof (PBE).[89] All of the calculations were performed with a plane-wave basis cutoff energy of 350 eV, a Monkhorst-Pack k-point mesh with 2400 k points per reciprocal atom, and a Gaussian smearing of the electronic occupancy with a width of 0.1 eV. Formation energies were converged to within 1 meV/cation with respect to cutoff energies and k-point meshes. Unless explicitly noted, total energies of all structures were minimized with respect to unit cell shape and volume, as well as atomic internal coordinates.

IV. RESULTS

A. Structure and geometry of IV–VI rocksalt alloys and compounds

We begin by discussing the lattice parameters of all IV–VI compounds and solutions. This quantity is easily compared with experiment, helping to validate our DFT calculations, and also defines the lattice mismatch of each system, which is critical in evaluations of the coherency strain energy (shown subsequently). We have calculated DFT total energies and relaxed geometries for PbS, PbTe, PbSe, SnTe, and GeTe in the rocksalt structure. In addition, we have calculated total energies and relaxed geometries for 32 atom (16 mixing atoms) rocksalt SQSs for the three anion-mixing pseudobinary systems Pb(S,Te), Pb(Te,Se), and Pb(Se,S), and the three cation-mixing pseudobinary systems (Pb,Sn)Te, (Sn,Ge)Te, and (Ge,Pb)Te. From these calculations, we can determine the lattice parameters of each system as a function of composition. Because of the low symmetry of the SQSs, and, in particular, the triclinic unit cells of these structures, an "average lattice parameter" was calculated by taking the cube root of the volume of eight atoms (the size of the conventional rocksalt unit cell) for each structure, $a_{SQS} = \sqrt[3]{V_{SQS}/4}$. This average lattice parameter allows a direct comparison with Vegard's law[90] as well as previous DFT calculations. Figures 3 and 4 show the lattice parameters for the anion- and cation-mixing systems as functions of composition, respectively. There is very little deviation from Vegard's law[90] in the random alloys of these systems. The largest deviations occur in (Ge,Pb)Te, where there is a slight upwards bowing of the lattice parameter

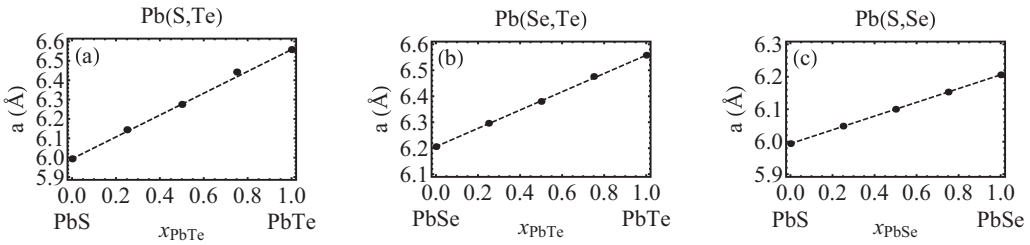

FIG. 3. DFT lattice parameters of anion-mixing systems (a) Pb(S,Te), (b) Pb(Te,Se), and (c) Pb(Se,S), as functions of composition. We give lattice parameters for the rocksalt compounds and three SQSs at $x = 1/4,1/2,3/4$ as models of the solid solution. Dashed lines show the linear dependence of lattice parameter on composition (Vegard's law) for each system. We find no appreciable deviation from Vegard's law in the solid solutions of these mixing systems.

from Vegard's law. This deviation is related to the relaxation of the (Ge,Pb)Te SQS away from the rocksalt structure and towards the low temperature rhombohedral structure of GeTe, as will be discussed in Sec. IV D. A comparison of our lattice parameter calculations with previous DFT calculations, as well as available experimental data, is shown in Table II.

B. Coherency strain and mixing energies for IV–VI rocksalt alloys and compounds

Next, we will construct all of the contributions to the free energy model of Sec. II. The resulting incoherent and coherent free energies of mixing will be used to calculate phase diagrams in Sec. IV C. We also calculate ordered structures in each of the alloy systems to investigate the short-range order of these systems.

1. Coherency strain energies

We calculate coherency strain energies for all of the pseudobinary rocksalt systems along three high symmetry directions: [100], [110], and [111]. In a cubic crystal with harmonic elasticity, the strain energies will have extrema along the [100] and [111] directions.[83] For some systems [e.g., Pb(S,Te) and(Ge,Pb)Te], the lattice mismatch is large, and anharmonic effects can be important. Our DFT calculations do not rely on any harmonic approximations, and anharmonic strain energies are directly incorporated in Eq. (8). For each system along each direction, we have calculated the epitaxial strain energy, $\Delta E_i^{\text{epi}}(\hat{k},a_\perp)$ of each constituent at five values of the lattice parameter $a_\perp$ perpendicular to the direction $\hat{k}$ (epitaxial lattice parameter). For each value of $a_\perp$, we minimize the energy of the structure with respect to the lattice parameter $a_\parallel$ along the direction $\hat{k}$, while keeping the lattice parameter $a_\perp$ fixed. Figures 5 and 6 show the resulting coherency strain energies for all of the systems considered along the [100] and [111] directions.

The thermal expansion coefficients of the IV–VI rocksalt compounds are relatively large,[67,118] and, in principle, this thermal expansion could introduce large temperature dependencies into the coherency strain energies. However, the effect that is important for coherency strain energies is not the absolute change in lattice parameter of a compound with temperature but the change in lattice mismatch between two compounds with temperature. For Pb(S,Te), the system with the largest lattice mismatch considered here, the change in mismatch with temperature is very small[67,118] (8.98% at zero Kelvin using our calculated lattice parameters and 9.03% at 1000 K including the experimental thermal expansion coefficients in Ref. 118), and we estimate the increase in the coherency strain energy of Pb(S,Te) due to thermal expansion to be less than 3 meV/cation at 1000 K using the thermal expansion data of Ref. 67 or 118.

2. Mixing enthalpies

The formation enthalpies of pseudobinary SQSs relative to pure rocksalt constituents (incoherent phase separation) are shown in Fig. 5 (anion mixing systems) and Fig. 6 (cation mixing systems), along with a subregular solid solution model mixing enthalpy curve (fit to the SQSs) and coherency strain energies along [100] and [111]. Fitting parameters for each system are included in Table I. In the anion mixing systems, the coherency strain energies along [111] all lie below both the coherency strain curves along [100] and the

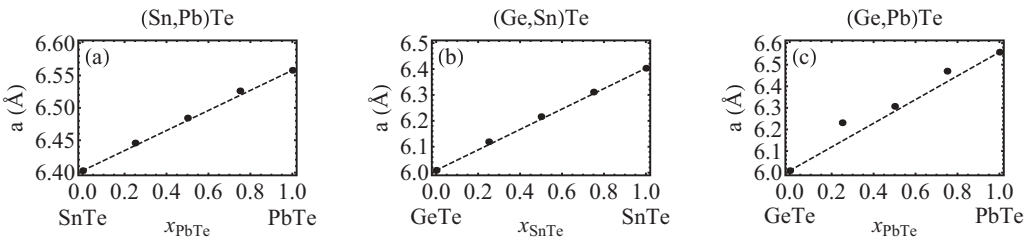

FIG. 4. DFT lattice parameters of cation-mixing systems (a) (Pb,Sn)Te, (b) (Sn,Ge)Te, and (c) (Ge,Pb)Te, as functions of composition. We give lattice parameters for the rocksalt compounds and three SQSs at $x = 1/4,1/2,3/4$ as models of the solid solution. Dashed lines show the linear dependence of lattice parameter on composition (Vegard's law) for each system. We find no appreciable deviation from Vegard's law in the solid solutions of these mixing systems except in the system (Ge,Pb)Te, where there is some positive deviation at compositions of 0.25 and 0.75 mole fraction PbTe.

TABLE II. Comparison of lattice parameter data for IV–VI pseudobinary rocksalt alloys. The lattice parameters calculated in this work are presented, along with literature data for DFT calculations made within the generalized gradient approximation (GGA)[53,57,59,61,62] and the local density approximation (LDA),[50,53,57,59] as well as experimental lattice parameters for each binary compound.[20,91] The empirical trend of LDA to overbind (smaller lattice parameter than experiment) and GGA to underbind (larger lattice parameter than experiment) is found for all the binary compounds.

		Lattice Parameter (Å)						
		Present DFT	Previous DFT					
	x	GGA	GGA			LDA		Experiment	
$PbS_{1-x}Te_x$	0	5.994	6.010[61]		6.012[59]	5.854[59]	5.906[50]	5.9362[91]	5.936[20]
	0.25	6.144	6.188[61]		6.14[a,59]	5.96[a,59]			
	0.5	6.275	6.325[61]		6.29[a,59]	6.10[a,59]			
	0.75	6.442	6.450[61]		6.44[a,59]	6.23[a,59]			
	1	6.558	6.560[61]		6.570[59]	6.383[59]	6.439[50]	6.4603[91]	6.454[20]
$PbTe_{1-x}Se_x$	0	6.558	6.560[61]		6.570[59]	6.383[59]	6.439[50]	6.4603[91]	6.454[20]
	0.25	6.476	6.487[61]		6.50[a,59]	6.30[a,59]			
	0.5	6.380	6.406[61]		6.40[a,59]	6.22[a,59]			
	0.75	6.296	6.320[61]		6.31[a,59]	6.13[a,59]			
	1	6.206	6.210[61]		6.222[59]	6.046[59]	6.098[50]	6.1243[91]	6.124[20]
$PbSe_{1-x}S_x$	0	6.206	6.2105[61]	6.224[62]	6.222[57]	6.053[57]	6.098[50]	6.1243[91]	6.124[20]
	0.25	6.153	6.1795[61]	6.174[62]	6.174[57]	5.998[57]			
	0.5	6.100	6.1285[61]	6.125[62]	6.122[57]	5.954[57]			
	0.75	6.048	6.0735[61]	6.071[62]	6.069[57]	5.905[57]			
	1	5.994	6.0105[61]	6.011[62]	6.012[57]	5.854[57]	5.906[50]	5.9362[91]	5.936[20]
$Pb_{1-x}Sn_xTe$	0	6.558		6.570[59]		6.439[50]		6.4603[91]	6.454[20]
	0.25	6.526							
	0.5	6.484							
	0.75	6.446							
	1	6.403		6.404[53]		6.231[53]		6.313[20]	
$Sn_{1-x}Ge_xTe$	0	6.403		6.404[53]		6.231[53]		6.313[20]	
	0.25	6.311							
	0.5	6.216							
	0.75	6.119							
	1	6.009		6.011[53]		5.858[53]		5.996[20]	
$Ge_{1-x}Pb_xTe$	0	6.009		6.011[53]		5.858[53]		5.996[20]	
	0.25	6.231							
	0.5	6.307							
	0.75	6.470							
	1	6.558		6.570[59]		6.439[50]		6.4603[91]	6.454[20]

[a]Data extracted from Fig. 1 of Ref. 59.

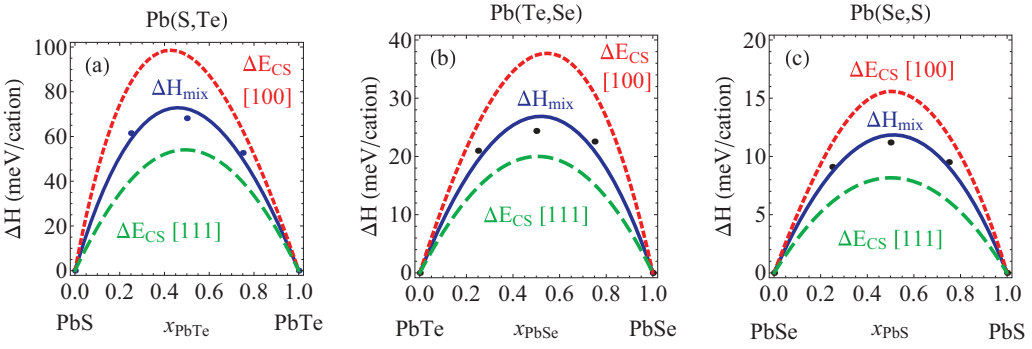

FIG. 5. (Color online) Solid solution subregular mixing enthalpies (blue solid line), and coherency strain energy curves along [100] (red dotted line) and [111] (green dashed line) for the anion mixing systems (a) Pb(S,Te), (b) Pb(Te,Se), and (c) Pb(Se,S). Subregular solution models were fit to the formation enthalpies of SQSs at concentrations of 0.25, 0.5, and 0.75 mole fractions (black points). All enthalpies are given with respect to incoherent phase separation.

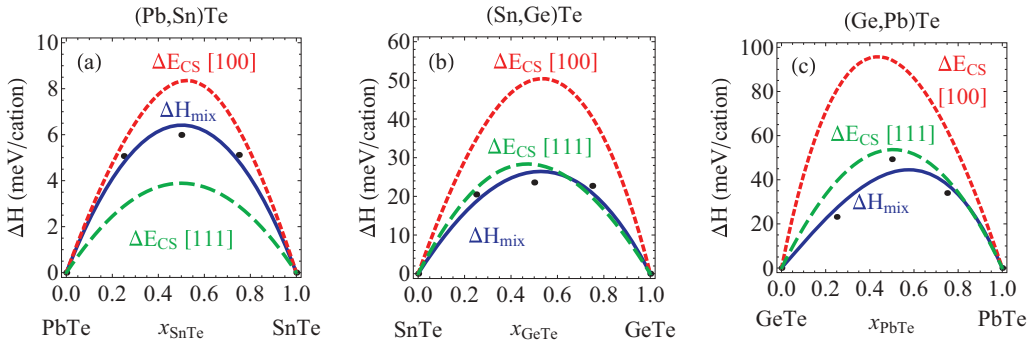

FIG. 6. (Color online) Solid solution subregular mixing enthalpies (blue solid line), and coherency strain energy curves along [100] (red dotted line) and [111] (green dashed line) for the cation mixing systems (a) (Pb,Sn)Te, (b) (Sn,Ge)Te, and (c) (Ge,Pb)Te. Subregular solution models were fit to the formation enthalpies of SQSs at concentrations of 0.25, 0.5, and 0.75 mole fractions (black points). All enthalpies are given with respect to incoherent phase separation.

solid solution mixing enthalpy curves. However, in the cation mixing systems, the solid solution mixing enthalpy curves lie below the coherency strain energy curve along [111] for a majority of the composition range in the (Sn,Ge)Te and (Ge,Pb)Te systems. This is due to the fact that the SQSs can locally relax towards the rhombohedral structure, while atomic relaxations in the coherency strain calculations are constrained by the inversion center of the rocksalt structure.

From the results of Figs. 5 and 6 we can make several observations. First, the mixing enthalpies for every system are positive, consistent with the observed phase separation in these systems. Second, the thermodynamic driving force for incoherent phase separation ($\Delta H_{\text{mix}}^{\text{incoh}}$)—the difference between the solid solution curve and incoherent phase separation curve (x axis)—is greater in all cases than the thermodynamic driving force for coherent phase separation ($\Delta H_{\text{mix}}^{\text{coh}}$), which is the difference between the solid solution curve and the coherent phase separation curve (along [111]). This difference between the driving forces for incoherent and coherent phase separation will impact the corresponding incoherent miscibility gap and coherent spinodal temperatures in the phase diagrams we calculate. Finally, the coherency strain energies, even along the elastically softest direction [111], are significant fractions of the total mixing enthalpies, indicating that the coherency strain energies will greatly impact the phase stability of the IV–VI alloys and ignoring these energies will lead to unphysical estimates of coherent spinodals.

3. *Ordered structure formation enthalpies*

The coherent phase diagram of a system can be quite distinct from the equilibrium, incoherent phase diagram. Even in (incoherently) phase separating systems, it is possible for the coherent phase diagram to exhibit ordering.[27] In such systems, ordered structures exist which are higher in energy than incoherent phase separation but lower in energy than coherent phase separation. Many tetrahedral zinc-blende-based III–V semiconductor alloys (e.g., $Ga_xIn_{1-x}P$) exhibit this incoherent phase separating/coherent phase separating/ordering tendency.[35] But, coherent phase stability in octahedral rocksalt IV–VI alloys has not been investigated. To investigate this possibility of coherent ordering in the IV–VI rocksalt alloys, formation enthalpies of rocksalt-based ordered structures were calculated for each of the pseudobinary systems,

$$\Delta H_F^{\text{ord}}(\vec{k},x) = E_{\text{ord}}(\vec{k},x) - (1-x)E_{AC} - xE_{BC}, \quad (16)$$

where E_{ord} is the DFT energy per cation of the ordered structure with concentration x and composition wavevector $\vec{k}$. The formation enthalpies of these ordered structures combined with the coherency strain energy at the same x and $\hat{k}$ can be used to investigate the incoherent and coherent tendency toward ordering of the IV–VI systems. The formation enthalpies of ordered structures can also be decomposed into strain and chemical contributions, which give insight into the physical contributions of mixing in a system.

The ordered structures considered here all have pseudobinary mole fractions of 0.5 and composition wavevectors along either [100] or [111]. That is to say, these ordered structures are all $(AC)_p(BC)_p$ superlattices of period p oriented along $\hat{k} = [100]$ or [111]. The formation enthalpies of these ordered structures, SQSs, and coherency strain energies are listed for each pseudobinary system in Table III. Figure 7 compares these various formation and coherency strain energies at 0.5 mole fraction for each pseudobinary system by normalizing energies by the coherency strain energy along [111] at 0.5 atomic fraction of each system. This normalization is done to allow a more direct comparison of the relative ordering of the various structures across each system.

The incoherent phase stability of a system is determined by the lowest energy state accessible to the system out of all possible states, including incoherent phase separation.[27] On the other hand, the coherent phase stability of a system is determined by the lowest energy state possible at a fixed volume, i.e., excluding incoherent phase separation but including coherent phase separation.[27] Figure 7 shows the energetic competition between ordered compounds, coherent phase separation, and incoherent phase separation in each system. From Fig. 7 we can see that the lowest energy state for all of the IV–VI systems is incoherent phase separation. However, for coherent phase stability, we ignore incoherent phase separation and consider the relative energies of all the other states in Fig. 7. We see that the anion mixing systems and the Ge-containing cation mixing systems [Pb(S,Te), Pb(Te,Se), Pb(Se,S), (Sn,Ge)Te, and (Ge,Pb)Te] all have ordered structures as their lowest

TABLE III. Formation energies of structures ordered along [100] and [111] for each of the pseudobinary systems. The formation energies are all with respect to the rocksalt structures of each constituent binary compound in the pseudobinary system.

	Formation Energy of Ordered Structures (meV/cation)					
	Pb(S,Te)	Pb(Te,Se)	Pb(Se,S)	(Pb,Sn)Te	(Sn,Ge)Te	(Ge,Pb)Te
$(AC)_1(BC)_1$ [100]	174.8	66.3	26.3	11.2	61.7	134.2
$(AC)_2(BC)_2$ [100]	109.1	42.5	17.1	8.7	43.5	90.6
$(AC)_1(BC)_1$ [111]	45.7	14.7	7.9	6.3	14.2	36.6
$(AC)_2(BC)_2$ [111]	47.2	16.0	7.5	5.2	19.2	41.4
SQS-16 $x = 0.25$	61.5	21.0	9.1	5.1	20.5	23.2
SQS-16 $x = 0.5$	68.2	24.4	11.2	6.0	23.6	49.3
SQS-16 $x = 0.75$	52.7	22.6	9.5	5.1	22.71	34.0
ΔE_{CS} ([100], $x = 0.5$)	96.4	37.4	15.6	8.3	50.2	94.2
ΔE_{CS} ([111], $x = 0.5$)	54.0	20.0	8.2	3.9	28.3	53.7

energy coherent states. This behavior can be contrasted by (Pb,Sn)Te, where the lowest energy coherent state (excluding incoherent phase separation) is coherent phase separation. Thus, all of the IV–VI systems except (Pb,Sn)Te have a preference for metastable coherent ordering over coherent phase separation (and hence spinodal decomposition) at low temperatures. This competition between coherent ordering and phase separation is explored more thoroughly for the system Pb(S,Te) in ongoing work.[92]

In addition to determining the incoherent and coherent phase stability of these systems, the ordered structures can give us insight into the chemical and strain contributions to the mixing enthalpies in each of the rocksalt systems. The coherency strain energy along a specific direction, $\hat{k}$, is the strain energy of $(AC)_p(BC)_p$ stacking along $\hat{k}$ in the limit as $p \to \infty$. Thus the difference between an ordered structure with finite stacking along $\hat{k}$, Eq. (16), and the coherency strain energy along $\hat{k}$, Eq. (9), gives a quantity we define as the chemical energy of the ordered structure,[26]

$$\Delta E_{\text{chem}}(\vec{k},x) \equiv \Delta H_F^{\text{ord}}(\vec{k},x) - \Delta E_{CS}(\hat{k},x). \tag{17}$$

This chemical energy indicates whether, in the absence of strain, the system prefers unlike A-B pairs (negative chemical energy) or like A-A + B-B pairs (positive chemical energy). From Fig. 7 we can see that the coherency strain energies of both cation- and anion-mixing systems are lowest along the [111] direction and highest along the [100] direction. In the anion-mixing system the chemical energy is highly direction dependent, with the [100] direction having a positive chemical energy (difference between $(AC)_1(BC)_1$[100] or $(AC)_2(BC)_2$[100] and C.P.S. [100]), and the [111] direction having a negative chemical energy (difference between $(AC)_1(BC)_1$[111] or $(AC)_2(BC)_2$[111] and C.P.S. [111]). Thus there is a preference for A-B pairs along [111], but A-A and B-B pairs along [100], which is highly unusual. The

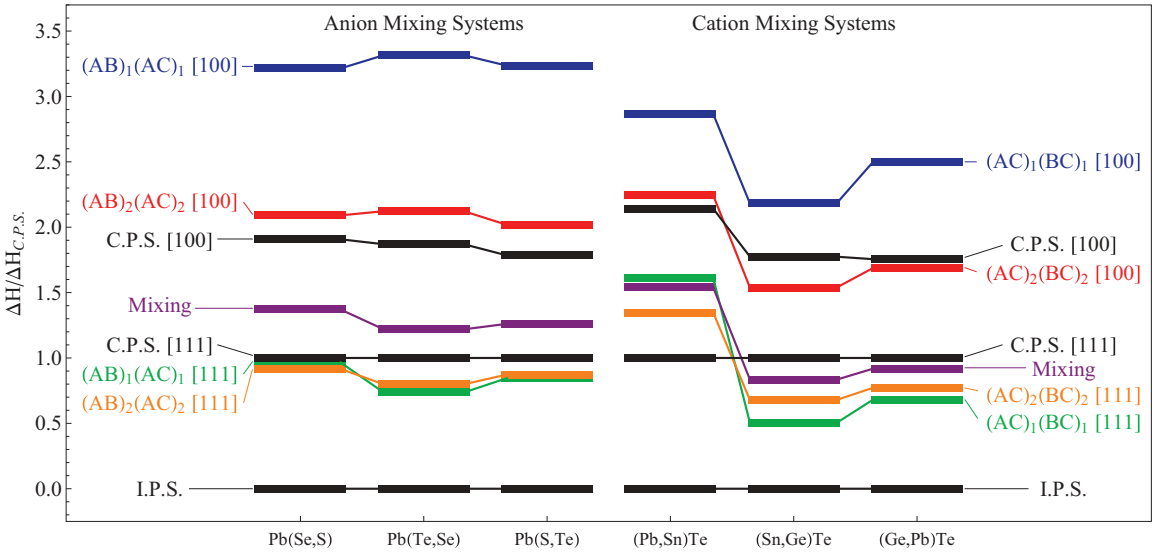

FIG. 7. (Color online) DFT energies of ordered structures of IV–VI systems, scaled by the coherency strain energy along [111] of each system (C.P.S. [111]). Lines are provided as a guide to the eye. The stable long-range order for all systems is incoherent phase separation (IPS). Ignoring IPS and considering the relative energetics of all other structures exposes the preferred coherent phase stability. Structures ordered along [100] have the highest energies for all systems, while structures ordered along [111] have the lowest energies for all systems [except (Pb,Sn)Te, which has coherent phase separation as its lowest], indicates that these systems [except (Pb,Sn)Te] should order before coherently phase separating.

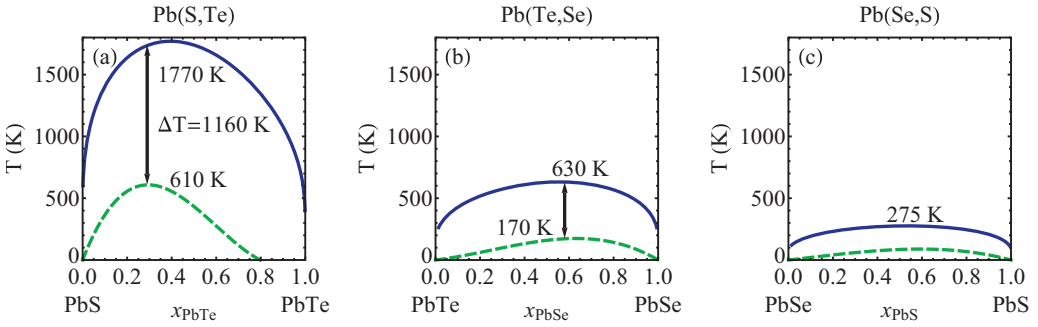

FIG. 8. (Color online) Incoherent miscibility gaps (solid blue lines) and coherent spinodal lines (dashed green) for the anion sublattice mixing systems.

anion-mixing system can be contrasted with the cation-mixing system [except (Pb,Sn)Te, which has extremely low formation enthalpies], where, along the [100] direction, the chemical energy changes sign from positive to negative between one- and two-period superlattices. In these cation-mixing systems, the random mixing enthalpies also lie below the coherency strain energies along both [111] and [100], indicating that the mixing enthalpies also have negative chemical energies.[93]

C. Phase diagrams of IV–VI rocksalt alloys

Now that we have assembled all of the energetic input to our thermodynamic model, we combine this with the ideal mixing entropy term to compute incoherent miscibility gaps and coherent spinodals for each pseudobinary system. These are shown in Figs. 8 and 9 for the anion mixing and cation mixing systems, respectively.

1. Comparison with experiment for Pb(S,Te)

Comparing the calculated incoherent miscibility gap of Pb(S,Te) in Fig. 8(a) with the experimental miscibility gap,[17] we find that qualitatively the overall topology and asymmetry of the experimental phase diagram is captured by our model. However, quantitatively the maximum temperature of the calculated miscibility gap is a factor of 1.7 higher than that of the experimental gap. Overestimation of the temperature scale of phase boundaries from DFT data is common,[23–25,35,94] when not all of the sources of mixing entropy are accounted for. In this model, the only temperature dependence in the free energy of mixing comes from the ideal mixing entropy. There are several additional sources of excess mixing entropy, which can have large effects on the free energy and resulting miscibility gap. These include the nonideal configurational entropy,[24,35,95] electronic entropy of mixing,[32] and vibrational entropy of mixing.[33]

Due to the semiconducting nature of these materials, the electronic entropy is expected to be small, and the electronic entropy of mixing small enough to be neglected. We expect the vibrational entropy of mixing to be significant due to the large lattice mismatch in Pb(S,Te) and the anharmonic nature of phonons in PbTe.[96] Preliminary DFT frozen phonon calculations on the Pb(S,Te) SQS's show that including the vibrational entropy of mixing in the free energy of Pb(S,Te) reduces the calculated incoherent miscibility gap, bringing the calculation into better agreement with the experimental miscibility gap. These vibrational entropy calculations will be reported in a forthcoming paper.[97]

2. Depression of the coherent spinodal

We next examine the coherent spinodals. By comparing the maximum temperature of the coherent spinodal with that of the incoherent miscibility gap, we see the magnitude of the depression of the spinodal due to coherency strain. From Figs. 8 and 9 we can see that the requirement of coherent phase separation does indeed significantly depress the maximum spinodal temperature from the top of the incoherent miscibility gap, in most cases by a factor of 3 or more. Table IV shows the calculated incoherent miscibility gap and coherent spinodal temperatures, as well as experimental miscibility gap temperatures, where available.

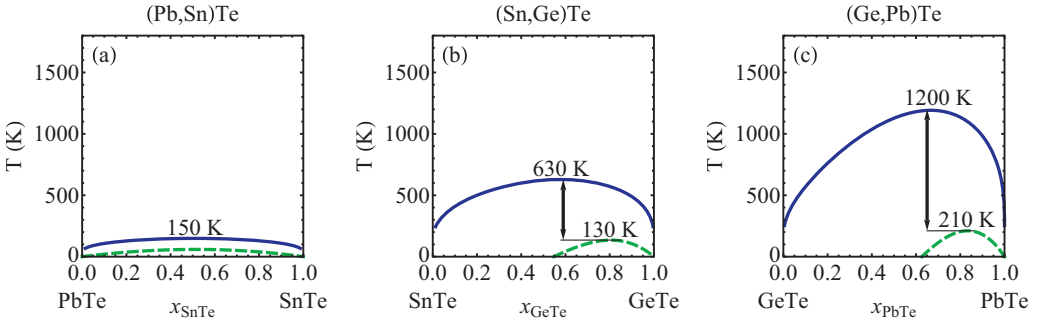

FIG. 9. (Color online) Incoherent miscibility gaps (solid blue) and coherent spinodal lines (dashed green) for the cation sublattice mixing systems.

TABLE IV. Incoherent miscibility gap and coherent spinodal heights calculated with the subregular solution model are compared with experimental miscibility gap heights, where available. We also compare with previous DFT work on Pb(Se,S), which uses a regular-solution model. The previous DFT calculations of Boukhris *et al.*[61] are not included due to an error in their calculation of miscibility gap temperatures.[98]

		T_c Incoh (K)	x_c Incoh	T_c coh (K)	x_c coh	T_c Incoh − T_c coh (K)
Pb(S,Te)	Exp.[15,17,18]	1070	0.4			
	Present Work	1770	0.40	610	0.30	1160
Pb(Te,Se)	Exp.[18]	–	–			
	Present work	630	0.56	170	0.63	
Pb(Se,S)	Exp.[18,72]	–	–			
	Present work	275	0.53	90	0.60	
	Previous DFT	290[62]	0.5	–	–	–
(Pb,Sn)Te	Exp.[75]	–	–			
	Present work	150	0.51	60	0.51	90
(Sn,Ge)Te	Exp.[77]	540	0.5			
	Present work	630	0.58	130	0.80	500
(Ge,Pb)Te	Exp.[77,78]	845	0.6			
	Present work	1200	0.67	210	0.83	990

We find that the coherent spinodal of Pb(S,Te) is depressed by 1160 K from the incoherent miscibility gap, meaning spinodal decomposition is only possible at low temperatures where it is kinetically inaccessible in Pb(S,Te). The same conclusion can be made for (Ge,Pb)Te, where the spinodal is depressed by 990 K from the miscibility gap. For the other IV–VI systems, the coherent spinodals occur at low enough temperatures that the solid solution should be (meta)stable at any processing temperature. Furthermore, as indicated by the formation enthalpies of ordered compounds in these systems, the coherent diagrams of these systems should show ordering, not decomposition.

3. *Physical contributions to miscibility gap temperatures: Dominant role of strain*

We next illustrate trends in the calculated incoherent and coherent miscibility gap heights to better understand the physical contributions underlying phase separation in these alloy systems. We find that the incoherent miscibility gap temperature of the IV–VI pseudobinary systems scale with the coherency strain energies of the systems, as shown in Fig. 10. While we have used a subregular solution model to calculate the miscibility gaps in these systems, the strain energy dependence of the incoherent miscibility gap can be shown analytically for a regular solution model.

In a regular solution model, there is one interaction parameter in the excess mixing enthalpy,

$$\Delta H_{\text{mix}} = \omega x(1-x), \tag{18}$$

as well as the ideal mixing entropy from Eq. (8). The miscibility gap height of a regular solution model can be found analytically and is located at a composition of 0.5 mole fraction, given by

$$T_c = \frac{2\Delta H_{\text{mix}}}{k_B} = \frac{\omega}{2k_B}. \tag{19}$$

If some fraction, γ, of the enthalpy of mixing is due to strain energy,

$$\Delta H_{\text{mix}} = \gamma \Delta E_{CS}, \tag{20}$$

then there is a linear dependence of T_c on the strain energy,

$$T_c = \frac{2\gamma \Delta E_{CS}}{k_B}, \tag{21}$$

with a proportionality constant of $\frac{2\gamma}{k_B}$. This line is plotted in Fig. 10 for the case of $\gamma = 1$, which corresponds to a system that interacts only through strain. The cation sublattice mixing systems are almost perfectly described by this strain-only model, whereas the anion sublattice mixing systems show some deviation, indicating a (small) effect of chemical bonding on T_c for these systems. For all systems, the strain energy is the dominant contribution to mixing.

D. SQS bond lengths and distortions

In addition to energetics of solid solutions, our SQS calculations provide a means to investigate the local atomic environment in a disordered solid. Relaxation around each atom in the alloy break the symmetry of the parent lattice and can contribute to the energies and other properties of the solid solution.[82] Even in solid solutions obeying Vegard's law,

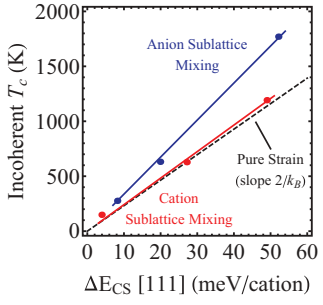

FIG. 10. (Color online) Plot of calculated incoherent miscibility gap temperature, T_c, for each pseudobinary system versus the coherency strain energy, $\Delta E_{CS}^{\text{min}}$, in each system. A linear dependence of T_c on $\Delta E_{CS}^{\text{min}}$ is found for the anion- (blue/medium gray) and cation-sublattice (red/dark gray) mixing systems. The dashed line shows how a regular solution model system consisting of only strain interactions would behave.

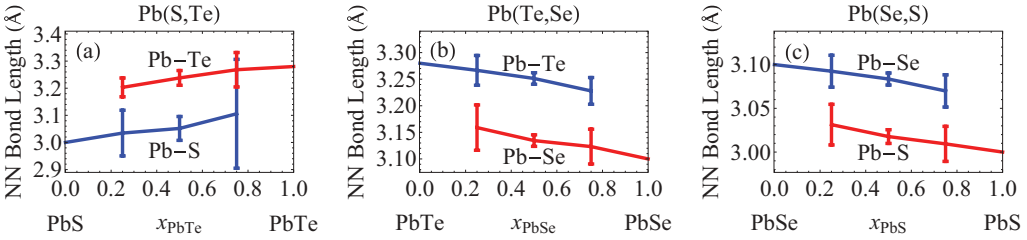

FIG. 11. (Color online) SQS average nearest-neighbor bond lengths for the anion-mixing system.

relaxations on the atomic scale can allow nearest neighbor atoms to take on bond lengths close to those of the constituent compounds.

1. SQS bond lengths

Figures 11 and 12 show the average nearest-neighbor bond lengths of the anion and cation mixing systems, respectively. Vertical bars show the standard deviations of these bond lengths. From these plots, we can see that, generally speaking, the nearest-neighbor bond lengths do not deviate much from those of the constituent rocksalt compounds. Thus, even in the solid solution, the local bond lengths of A-B and A-C bonds deviate significantly from the average bond lengths; there are significant local relaxations from the ideal rocksalt structure in the solid solutions. We also note that large standard deviations occur for two systems, Pb(S,Te) and (Ge,Pb)Te, the two systems with the largest lattice mismatch.

In Fig. 13, the distribution of Pb-S nearest-neighbor bonds are plotted as a function of bond length for all three of the SQSs. The Pb-S bonds in the Te-rich SQS have a much broader distribution, with some of the Pb-S bonds being forced into a Pb-Te-like environment. Furthermore, in the 0.75 mole fraction PbTe SQS, there is a single outlying Pb-S bond with a length larger than the Pb-Te bond length in PbTe, which creates the large standard deviation found in Fig. 11(a). This bimodal distribution of Pb-S nearest-neighbor bonds found in the Pb(S,Te) SQSs is consistent with the results of a previous calculation of bonding in this system using SQS-8.[50]

The large standard deviations in the Ge-Te bond lengths found in the (Ge,Pb)Te system occur because the Ge-Te bonds relax towards the bond lengths of the rhombohedral GeTe ground-state structure. This relaxation can be seen in Fig. 14, where the distribution of Ge-Te nearest-neighbor bond lengths are shown for each of the (Ge,Pb)Te SQSs. As the mole fraction of GeTe increases, the distribution of Ge-Te bonds becomes bi-modal and shifts towards the nearest-neighbor bond length of Ge-Te in the rhombohedral GeTe structure. At 0.75 mole fraction GeTe, the distribution of Ge-Te bonds has maxima centered over the rhombohedral GeTe bond length and the rocksalt PbTe bond length. As a test of these ideas, we replaced the Pb atoms with Ge atoms in the relaxed $Ge_{0.25}Pb_{0.75}Te$ SQS, and rerelaxed it. This hypothetical $Ge_{0.25}Ge_{0.75}Te$ structure relaxed completely to the rhombohedral GeTe structure instead of the initial rocksalt lattice, indicating that the energy barrier between rocksalt and rhombohedral GeTe had been overcome by the local relaxations in the SQS.

2. Distortions from rocksalt

Many of the compounds in the IV-VI rocksalt family undergo ferroelectric distortions from rocksalt to a rhombohedral structure at low temperatures. These systems include GeTe,[99,100] SnTe,[101,102] (Ge,Pb)Te,[103–105] (Sn,Ge)Te,[106] and (Pb,Sn)Te.[105] Furthermore, PbTe has a near-ferroelectric optical phonon mode, and both PbS and PbTe have been shown to undergo an off-centering of Pb ions with increasing temperature.[107] It has been proposed that Pb(S,Te) undergoes a ferroelectric distortion at low temperatures[108] due to a distribution of Pb-S bond lengths in the solid solution, though it has been pointed out that this distribution of bond lengths should be expected in the solid solution independent of any ferroeletric behavior[50] (as we have found in the current SQS bond lengths).

In this work, we have come across several distortions away from the rocksalt structure. In addition to the Ge-Te distortions discussed previously, we have found that when PbTe is coherently strained to the lattice parameter of PbS along [100] it will undergo a buckling distortion where Pb and Te atoms alternatingly move along [100] or [$\bar{1}$00]. This distortion lowers the energy of the PbTe cell by 92 meV/cation relative to the coherently strained cell with atoms on their ideal lattice sites. This highly strained state is still 437 meV/cat higher in energy than the PbTe rocksalt ground state. A more

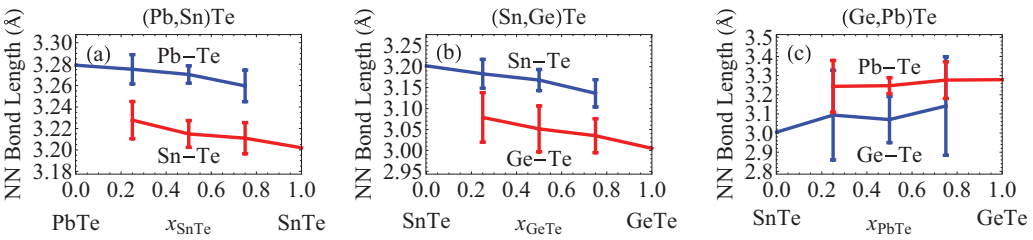

FIG. 12. (Color online) SQS average nearest-neighbor bond lengths for the cation-mixing systems. The large range bars in the Ge-Te bond lengths of the (Ge,Pb)Te system suggest that the system is trying to relax towards the rhombohedral GeTe structure.

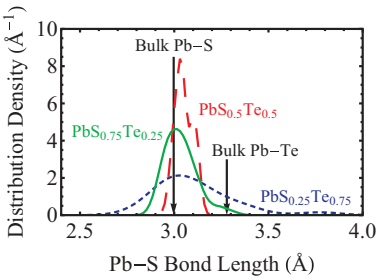

FIG. 13. (Color online) Pb-S bond lengths in Pb(S,Te) SQSs. Vertical lines show the Pb-S bond length in PbS (3.00 Å) and Pb-Te bond length in PbTe (3.25 Å). Solid (green), dashed (red), and dotted (blue) lines show the density of Pb-S bond lengths in the 0.25, 0.5, and 0.75 mole fraction PbTe SQSs, respectively. As the fraction of PbTe increases, the Pb-S bond distribution shifts towards the Pb-Te bond length. The large standard deviation in Fig. 11 can now be seen to come from the outlying Pb-S bond in the 0.75 mole fraction PbTe SQS.

in-depth analysis of this instability will be provided in a future publication.

Despite the large decrease in energy upon relaxing atomic positions, the distorted PbTe structure does not have a large effect on the coherency strain energy of Pb(S,Te). Because the distortion of PbTe sets in only at large strains corresponding to small concentrations of PbTe, the weight given to the decreased epitaxial strain energy according to Eq. (8) is very small, and the effect on the coherency strain energy of Pb(S,Te) along [100] is minimal and is neglected in the previous results.

V. DISCUSSION

Our results indicate that spinodal decomposition is not a kinetically accessible decomposition mechanism in any of the IV–VI rocksalt semiconductor alloys. In all cases, the largest portion of the thermodynamic driving force for incoherent phase separation comes from strain energy, which stabilizes the solid solution with respect to infinitesimal composition

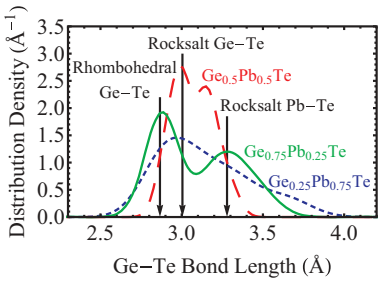

FIG. 14. (Color online) Ge-Te bond lengths in (Ge,Pb)Te SQSs. Vertical lines show the Ge-Te bond length in rhombohedral GeTe (2.87 Å), rocksalt GeTe (3.00 Å), and the Pb-Te bond length in PbTe (3.25 Å). Dotted (blue), dashed (red), and solid (green) lines show the density of Ge-Te bond lengths in the 0.25, 0.5, and 0.75 mole fraction GeTe SQSs, respectively. As the fraction of GeTe increases, the Ge-Te bond-length distribution shifts from a broad spread around the rocksalt bond lengths to a bimodal distribution with peaks centered on the rhombohedral GeTe bond length and the rocksalt PbTe bond length.

fluctuations, and is not part of the driving force for coherent phase separation. However, there is experimental evidence that spinodal decomposition occurs in the Pb(S,Te)[7,16] and (Ge,Pb)Te[76,78,109] systems. To explore this disagreement, we need to consider both the details of the experimental evidence and the theoretical foundations on which our claims are made.

Evidence for spinodal decomposition in Pb(S,Te) was seen by Darrow *et al.*[16] in the form of micrographs of lamellar phase separated structures with spacing on the order of 400–1000 Å. Sidebands were also found in the x-ray diffraction patterns of some of the quenched and aged samples.[16] In more recent studies of Pb(S,Te), striped and fringed structures with spacings on the order of nanometers were observed in transmission electron micrographs of slow-cooled Pb(S,Te) alloys.[7] In the system (Ge,Pb,Sn)Te, lamellar and fishbone structures have been observed that coarsen over time.[109] It should be noted that while sidebands are evidence of a modulated microstructure, these modulations do not need to be caused by spinodal decomposition. For instance, nonspinodal microstructures giving rise to sidebands have been found in aged Ni-Al alloys.[110]

In classical nucleation theory (CNT), there is an energy barrier to forming a precipitate, or nucleus, of a new phase that remains finite until the spinodal line is crossed. At this point, the energy barrier discontinuously drops to zero as the system becomes unstable to the precipitation of a second phase. This classical picture gives rise to the notion that nucleation and growth and spinodal decomposition are separate mechanisms of phase separation which evolve into very different microstructures. However, in the diffuse interface theory of phase separation, this is not the case.[95]

In the theory of phase separation proposed by Cahn in 1958,[111] precipitate geometry is not assumed *a priori* but is instead found by minimizing a free energy functional, which includes interfacial and strain effects.[111–113] This approach can be contrasted with the classical theory, which assumes a spherical precipitate with a homogenous, bulk composition, and infinitely sharp interface. In the diffuse interface theory, it is found that as the spinodal is approached, precipitate interfaces become much more diffuse, and the energy barrier continuously decreases to zero at the spinodal.[113] This more accurate treatment shows that nucleation and growth and spinodal decomposition are in fact two extremes of the same phase separation mechanism, and that microstructure is not an ideal way to distinguish between these two ends.

Despite the fact that the energy barrier to precipitation is a continuous function of composition and temperature throughout the miscibility gap, the existence or nonexistence of this barrier (apart from the barrier to diffusion) allows for a distinction between spinodal decomposition and nucleation and growth on the basis of kinetics. As discussed in Ref. 22, inside the spinodal the solid solution is unstable to infinitesimal composition fluctuations. In particular, composition fluctuations with some specific wavelength will grow faster than any other wavelength.[22] This microstructure evolution can be observed by *in situ* small angle x-ray scattering experiments and is a less ambiguous determination of spinodal decomposition than microstructure alone.

The model employed herein assumes a perfect, nondefected (albeit locally distorted) lattice for the solid solution and

coherently phase separated microstructures, and two different, noninteracting lattices for the incoherent phase separated microstructures. Lattice defects, such as dislocations and semicoherent interfaces, are not included in this model of phase separation. However, it has been shown through phase field modeling that dislocations can have large effects on both the kinetics and thermodynamics of coherent phase separation.[114–117] The elastic stresses of a dislocation can couple with the elastic stresses of composition change (in a lattice mismatched alloy) to cause phase separation outside the coherent miscibility gap[114] and increase the coherent spinodal temperature.[117]

In addition to ruling out spinodal decomposition as a possibility for the coherent phase diagrams of the IV–VI rocksalt alloys, our calculations suggest an alternative possibility: coherent ordering. In most of the systems considered [all except (Pb,Sn)Te], the ordered structure $(AC)_1(BC)_1[111]$ ($L1_1$ in Strukturbericht nomenclature, space group $R\bar{3}m$, number 166) is the lowest energy coherent phase at $x = 0.5$. This energetic preference indicates that inside the incoherent miscibility gap, there can exist a metastable coherent phase ordered along [111].

Similar to phase separation, ordering processes can occur by first- or second-order transformations. Symmetry can prevent some ordered structures from forming by continuous, second order processes, but the $(AC)_1(BC)_1[111]$ structure found lowest in energy in these systems is not one of them,[95] and the coherent phase diagram can show spinodal ordering from the random alloy to the coherently ordered phase.[95] The details of this coherent ordered phase diagram will be investigated in a future work.[92]

VI. CONCLUSIONS

In this study, we investigate the incoherent and coherent phase stability of IV–VI rocksalt semiconductor pseudobinary alloys using first-principles DFT calculations. We calculate the thermodynamic driving forces for incoherent and coherent phase separation using SQS and coherency strain energies, from which we obtain incoherent miscibility gaps and coherent spinodals. The large coherency strain energies of these systems dominate the thermodynamics, providing both the driving force for incoherent phase separation and suppressing coherent phase separation. In particular, for the systems Pb(S,Te) and (Ge,Pb)Te, the coherent spinodal is depressed in temperature to such a degree that spinodal decomposition should not be a kinetically accessible method of phase separation. In the other systems considered, the incoherent miscibility gaps are low enough in temperature that solid solutions are stable at processing temperatures. We further investigate competing types of coherent phase stability through calculations of ordered, superlattice structures. Structures ordered along [111] are found to have lower energies than the coherency strain energies for all systems except (Pb,Sn)Te, indicating that coherent ordering is more favorable than coherent phase separation for these systems.

In addition to energetics, we use the SQSs to study local atomic relaxations in the solid solutions of the IV–VI alloys. In all of the systems, the nearest neighbor A-C and B-C bond lengths of the solid solutions are close to those of the constituent compounds, showing that there are large deviations from the ideal rocksalt lattice in the solid solutions. In particular, for Pb(S,Te) and (Ge,Pb)Te, the systems with the largest lattice mismatch, a wide distribution of bond lengths occurred in the solid solutions, with the bonds of (Ge,Pb)Te showing distortions towards a rhombohedral GeTe structure.

Understanding the phase stability of the IV–VI rocksalt thermoelectric alloys is an important step towards controlling the thermoelectric efficiency of these alloys. To use coherent precipitates to improve the thermoelectric figure of merit, it is desirable to have an alloy system with two properties: (i) a high miscibility gap temperature to increase the number density of precipitates, and (ii) a small lattice mismatch between constituent compounds to maintain coherency between the precipitates and matrix. Our work here shows that, for the IV–VI rocksalt alloys, these two properties are coupled—strain between the constituent compounds is responsible for the incoherent phase separation but is also responsible for suppressing the coherent phase stability. In the search for thermoelectric alloy systems, our work shows that looking for systems where chemical effects, and not coherency strains, contribute to the immiscibility should constitute a promising strategy for finding systems with coherent nanoscale precipitates.

ACKNOWLEDGMENTS

This material is based upon work supported as part of the Revolutionary Materials for Solid State Energy Conversion, an Energy Frontier Research Center funded by the US Department of Energy, Office of Science, Office of Basic Energy Sciences under Award Number DE-SC00010543.

APPENDIX: COHERENT FREE-ENERGY FORMALISM—COMPARISON WITH CAHN[112] FORMULATION

The coherent free-energy model constructed here can be expressed in terms of the formalism used by Cahn.[112] A coherent free-energy density, φ, is constructed from the incoherent free energy density, f', by adding a strain-energy term,[112]

$$\varphi(x,x_0) = f'(x) + \frac{\eta^2 E}{1-\nu}(x-x_0)^2. \tag{A1}$$

The free-energy densities are per unit volume (a_0^3) of the average composition, x_0. The assumptions of this model are that the two phases have different equilibrium lattice parameters but the same elastic constants independent of concentration. Introducing a concentration dependence in the elastic constants would add higher order terms to Eq. (A1).

In analogy to Eq. (A1), we have our coherent free-energy density (per cation instead of volume),

$$\Delta G_{\text{mix}}^{\text{coh}}(x) = \Delta G_{\text{mix}}^{\text{incoh}}(x) - \Delta E_{CS}^{\text{min}}(x), \tag{A2}$$

with the coherency strain energy, $\Delta E_{CS}^{\text{min}}(x)$, given by Eq. (8). If we know the functional form of the coherency strain energy, we can fit Eq. (A2) into a form analogous to Eq. (A1). In this work, a subregular solution model is used to fit both the incoherent and coherent enthalpies of mixing, which is equivalent to the coherency strain energy having a subregular solution model functional form. We will examine the effects of using both

regular and subregular solution models for the coherency strain energy.

A regular solution model coherency strain energy (with interaction coefficient ω) gives us,

$$\Delta G^{\text{coh}}_{\text{mix}}(x) = \Delta G^{\text{incoh}}_{\text{mix}}(x) - \omega x(1-x), \tag{A3}$$

which can be rewritten as,

$$\Delta G^{\text{coh}}_{\text{mix}}(x) = \Delta G^{\text{incoh}}_{\text{mix}}(x) + \omega\,(x-x_0)^2 + \Omega_1(x-x_0) + \Omega_0, \tag{A4}$$

where Ω_1 and Ω_0 are functions of the average composition, x_0, and are given by

$$\Omega_1 = 2\omega x_0 - 1, \quad \Omega_0 = 2\omega x_0 - \omega x_0^2 - 1. \tag{A5}$$

As the chemical potentials of compounds AC and BC in a phase depend only on differences in the derivatives of the free energy, terms linear and constant in composition have no effect on the chemical potentials and correspond only to a change in reference states of compounds AC and BC. Thus, the last two terms in Eq. (A4) can be dropped to retain the same reference states in the coherent free energy that we have in the incoherent free energy. With this change, we recover the same form as Eq. (A1), find that ω is equal to the strain energy density, $\frac{\eta^2 E}{[1-\nu]}$, and see that the regular solution model form for the coherency strain energy corresponds to the model used by Cahn.

Using a subregular solution model coherency strain energy, we have

$$\Delta G^{\text{coh}}_{\text{mix}} = \Delta G^{\text{incoh}}_{\text{mix}} - \gamma x(1-x) - \delta x(1-x)(1-2x), \tag{A6}$$

which we can express as,

$$\Delta G^{\text{coh}}_{\text{mix}} = \Delta G^{\text{incoh}}_{\text{mix}} + Y_3(x-x_0)^3 + Y_2(x-x_0)^2 + Y_1(x-x_0) + Y_0, \tag{A7}$$

with coefficients,

$$\begin{aligned} Y_3 &= 2\delta, \\ Y_2 &= 6\delta x_0 - \gamma - 3\delta, \\ Y_1 &= 6\delta x_0^2 - 2\gamma x_0 - 6\delta x_0 + \gamma + \delta, \\ Y_0 &= 2\delta x_0^3 - \gamma x_0^2 - 3\delta x_0^2 + \gamma x_0 + \delta x_0. \end{aligned} \tag{A8}$$

Again, terms linear and constant in composition, x, can be neglected (corresponding to a change in reference states). This gives us an equation similar to Eq. (A1), with two significant differences: (i) there is a term cubic in composition difference and (ii) the coefficient of the quadratic term, Y_2, is dependent on the average composition, x_0. These differences are a result of elastic anharmonicity allowed in the coherency strain calculations[83] and have an effect on the coherent phase diagram as noted by Cahn;[112] the coherent phase boundaries will depend on the average composition of the alloy.

[1] Z. Dughaish, Physica B **322**, 205 (2002).
[2] T. C. Harman, P. J. Taylor, M. P. Walsh, and B. E. LaForge, Science **297**, 2229 (2002).
[3] K.-F. Hsu, S. Loo, F. Guo, W. Chen, J. S. Dyck, C. Uher, T. Hogan, E. K. Polychroniadis, and M. G. Kanatzidis, Science **303**, 818 (2004).
[4] J. P. Heremans, C. M. Thrush, and D. T. Morelli, J. Appl. Phys. **98**, 063703 (2005).
[5] J. Androulakis, K.-F. Hsu, R. Pcionek, H. Kong, C. Uher, J. J. D'Angelo, A. Downey, T. Hogan, and M. G. Kanatzidis, Adv. Mater. **18**, 1170 (2006).
[6] J. R. Sootsman, R. J. Pcionek, H. Kong, C. Uher, and M. G. Kanatzidis, Chem. Mater. **18**, 4993 (2006).
[7] J. Androulakis, C.-H. Lin, H.-J. Kong, C. Uher, C.-I. Wu, T. Hogan, B. A. Cook, T. Caillat, K. M. Paraskevopoulos, and M. G. Kanatzidis, J. Am. Chem. Soc. **129**, 9780 (2007).
[8] J. P. Heremans, V. Jovovic, E. S. Toberer, A. Saramat, K. Kurosaki, A. Charoenphakdee, S. Yamanaka, and G. J. Snyder, Science **321**, 554 (2008).
[9] B. Poudel *et al.*, Science **320**, 634 (2008).
[10] J. R. Sootsman, H. Kong, C. Uher, J. J. D'Angelo, C.-I. Wu, T. P. Hogan, T. Caillat, and M. G. Kanatzidis, Angew. Chem. Int. Ed. **47**, 8618 (2008).
[11] K. Biswas, J. He, Q. Zhang, G. Wang, C. Uher, V. P. Dravid, and M. G. Kanatzidis, Nat. Chem. **3**, 160 (2011).
[12] G. J. Snyder and E. S. Toberer, Nat. Mater. **7**, 105 (2008).
[13] J. R. Sootsman, D. Y. Chung, and M. G. Kanatzidis, Angew. Chem. Int. Ed. **48**, 8616 (2009).
[14] D. L. Medlin and G. J. Snyder, Curr. Opin. Colloid Interface Sci. **14**, 226 (2009).
[15] M. S. Darrow, W. B. White, and R. Roy, Trans. Metall. Soc. AIME **236**, 654 (1966).
[16] M. S. Darrow, W. B. White, and R. Roy, Mater. Sci. Eng. **3**, 289 (1968).
[17] V. Leute and N. Z. Volkmer, Phys. Chem. Neue Folge **144**, 145 (1985).
[18] V. Z. Leute, Naturforsch., A: Phys. Sci. **50**, 357 (1995).
[19] J. W. Cahn, Acta Metall. **9**, 795 (1961).
[20] M. L. Cohen and J. R. Chelikowsky, *Electronic Structure and Optical Properties of Semiconductors* (Springer-Verlag, Berlin, 1989).
[21] J. W. Cahn, Acta Metall. **10**, 179 (1962).
[22] J. W. Cahn, Trans. Metall. Soc. AIME **242**, 166 (1968).
[23] J. M. Sanchez, J. P. Stark, and V. L. Moruzzi, Phys. Rev. B **44**, 5411 (1991).
[24] C. Wolverton and A. Zunger, Comput. Mater. Sci. **8**, 107 (1997).
[25] V. Ozoliņš, C. Wolverton, and A. Zunger, Phys. Rev. B **57**, 6427 (1998).
[26] S. Muller, L.-W. Wang, A. Zunger, and C. Wolverton, Phys. Rev. B **60**, 16448 (1999).
[27] C. Wolverton, V. Ozoliņš, and A. Zunger, J. Phys.: Condens. Matter **12**, 2749 (2000).
[28] S. Muller, C. Wolverton, L.-W. Wang, and A. Zunger, Europhys. Lett. **55**, 33 (2001).
[29] M. Asta, V. Ozoliņš, and C. Woodward, JOM-J. Miner. Met. Mater. Soc. **53**, 16 (2001).
[30] C. Wolverton, Acta Mater. **49**, 3129 (2001).
[31] D. Shin, A. van de Walle, Y. Wang, and Z.-K. Liu, Phys. Rev. B **76**, 144204 (2007).
[32] C. Wolverton and A. Zunger, Phys. Rev. B **52**, 8813 (1995).

[33]V. Ozoliņš, C. Wolverton, and A. Zunger, Phys. Rev. B **58**, R5897 (1998).
[34]L. G. Ferreira, S.-H. Wei, and A. Zunger, Phys. Rev. B **40**, 3197 (1989).
[35]S.-H. Wei, L. G. Ferreira, and A. Zunger, Phys. Rev. B **41**, 8240 (1990).
[36]A. Silverman, A. Zunger, R. Kalish, and J. Adler, J. Phys.: Condens. Matter **7**, 1167 (1995).
[37]A. Silverman, A. Zunger, R. Kalish, and J. Adler, Phys. Rev. B **51**, 10795 (1995).
[38]L. K. Teles, J. Furthmuller, L. M. R. Scolfaro, J. R. Leite, and F. Bechstedt, Phys. Rev. B **62**, 2475 (2000).
[39]C. K. Gan, Y. P. Feng, and D. J. Srolovitz, Phys. Rev. B **73**, 235214 (2006).
[40]J. Liu and A. Zunger, Phys. Rev. B **77**, 205201 (2008).
[41]S. V. Barabash, V. Ozoliņš, and C. Wolverton, Phys. Rev. Lett. **101**, 155704 (2008).
[42]Y. Z. Zhu, G. D. Chen, H. Ye, A. Walsh, C. Y. Moon, and S.-H. Wei, Phys. Rev. B **77**, 245209 (2008).
[43]A. Predith, G. Ceder, C. Wolverton, K. Persson, and T. Mueller, Phys. Rev. B **77**, 144104 (2008).
[44]P. D. Tepesch, G. D. Garbulsky, and G. Ceder, Phys. Rev. Lett. **74**, 2272 (1995).
[45]G. Ceder, G. D. Garbulsky, and P. D. Tepesch, Phys. Rev. B **51**, 11257 (1995).
[46]D. Carlier, A. Van der Ven, C. Delmas, and G. Ceder, Chem. Mater. **15**, 2651 (2003).
[47]R. Malik, F. Zhou, and G. Ceder, Nat. Mater. **10**, 587 (2011).
[48]G. Martinez, M. Schluter, and M. L. Cohen, Phys. Rev. B **11**, 651 (1975).
[49]J. A. Valdivia and G. E. Barberis, J. Phys. Chem. Solids **56**, 1141 (1995).
[50]S.-H. Wei and A. Zunger, Phys. Rev. B **55**, 13605 (1997).
[51]E. A. Albanesi, C. Okoye, C. Rodriguez, E. Peltzer y Blanca, and A. Petukhov, Phys. Rev. B **61**, 16589 (2000).
[52]M. Lach-hab, D. A. Papaconstantopoulos, and M. J. Mehl, J. Phys. Chem. Solids **63**, 833 (2002).
[53]C. M. I. Okoye, J. Phys.: Condens. Matter **14**, 8625 (2002).
[54]R. Ahuja, Phys. Status Solidi B **235**, 341 (2003).
[55]K. Hummer, A. Grüneis, and G. Kresse, Phys. Rev. B **75**, 195211 (2007).
[56]I. V. Slipukhina and D. M. Bercha, Phys. Status Solidi B **244**, 650 (2007).
[57]S. Kacimi, A. Zaoui, B. Abbar, and B. Bouhafs, J. Alloys Compd. **462**, 135 (2008).
[58]T. Radzyński and A. Łusakowski, Acta Phys. Pol. A **116**, 954 (2009).
[59]A. Zaoui, S. Kacimi, M. Zaoui, and B. Bouhafs, Mater. Chem. Phys. **114**, 650 (2009).
[60]A. Svane, N. E. Christensen, M. Cardona, A. N. Chantis, M. van Schilfgaarde, and T. Kotani, Phys. Rev. B **81**, 245120 (2010).
[61]N. Boukhris, H. Meradji, S. Ghemid, S. Drablia, and F. El Haj Hassan, Phys. Scr. **83**, 065701 (2011).
[62]M. Labidi, H. Meradji, S. Ghemid, S. Labidi, and F. El Haj Hassan, Mod. Phys. Lett. B **25**, 473 (2011).
[63]K. Rabe and J. D. Joannopoulos, Phys. Rev. B **32**, 2302 (1985).
[64]M. Cardona, R. K. Kremer, R. Lauck, G. Siegle, J. Serrano, and A. H. Romero, Phys. Rev. B **76**, 075211 (2007).
[65]A. H. Romero, M. Cardona, R. K. Kremer, R. Lauck, G. Siegle, J. Serrano, and X. C. Gonze, Phys. Rev. B **78**, 224302 (2008).
[66]J. An, A. Subedi, and D. Singh, Solid State Commun. **148**, 417 (2008).
[67]Y. Zhang, X. Ke, C. Chen, J. Yang, and P. R. C. Kent, Phys. Rev. B **80**, 024304 (2009).
[68]L. Xu, Y. Zheng, and J.-C. Zheng, Phys. Rev. B **82**, 195102 (2010).
[69]Y. Bencherif, A. Boukra, A. Zaoui, and M. Ferhat, Infrared Phys. Technol. **54**, 39 (2011).
[70]A. A. Volykhov, L. V. Yashina, and V. I. Shtanov, Inorg. Mater. **42**, 596 (2006).
[71]J. Steininger, J. Appl. Phys. **41**, 2713 (1970).
[72]D. E. Grimes, Trans. Metall. Soc. AIME **233**, 1442 (1965).
[73]J. S. Harris, J. T. Longo, E. R. Gertner, and J. E. Clarke, J. Cryst. Growth **28**, 334 (1975).
[74]V. Z. Leute, Naturforsch., A: Phys. Sci. **50**, 459 (1995).
[75]U. Kattner, H. L. Lukas, G. Petzow, B. Gather, E. Irle, and R. Blachnik, Z. Metallkd. **79**, 32 (1988).
[76]L. Yashina, V. Leute, V. Shtanov, H. Schmidtke, and V. Neudachina, J. Alloys Compd. **413**, 133 (2006).
[77]L. Yashina and V. Leute, J. Alloys Compd. **313**, 85 (2000).
[78]D. K. Hohnke, H. Holloway, and S. Kaiser, J. Phys. Chem. Solids **33**, 2053 (1972).
[79]M. Massimo and I. B. Cadoff, J. Electron. Mater. **5**, 601 (1976).
[80]P. R. Shamsuddin, S. Misra, and T. R. Anantharaman, J. Mater. Sci. **10**, 1849 (1975).
[81]A. Zunger, S.-H. Wei, L. G. Ferreira, and J. E. Bernard, Phys. Rev. Lett. **65**, 353 (1990).
[82]S.-H. Wei, L. G. Ferreira, J. E. Bernard, and A. Zunger, Phys. Rev. B **42**, 9622 (1990).
[83]V. Ozoliņš, C. Wolverton, and A. Zunger, Phys. Rev. B **57**, 4819 (1998).
[84]A. van de Walle, M. Asta, and G. Ceder, Calphad **26**, 539 (2002).
[85]P. Hohenberg and W. Kohn, Phys. Rev. **136**, 864 (1964).
[86]W. Kohn and L. J. Sham, Phys. Rev. **140**, 1133 (1965).
[87]G. Kresse and J. Furthmüller, Phys. Rev. B **54**, 11169 (1996).
[88]P. E. Blöchl, Phys. Rev. B **50**, 17953 (1994).
[89]J. P. Perdew, K. Burke, and M. Ernzerhof, Phys. Rev. Lett. **77**, 3865 (1996).
[90]L. Z. Vegard, Phys. **5**, 17 (1921).
[91]R. Dalvin, Solid State Phys. **28**, 179 (1973).
[92]W. A. Counts and C. Wolverton (unpublished).
[93]The strain energy of the random alloy is actually a weighted average of the coherency strain energy along all directions in the first Brillouin zone, but for an elastically harmonic alloy this average must fall between the coherency strain energies along [100] and [111].
[94]C. Ravi, C. Wolverton, and V. Ozoliņš, Europhys. Lett. **73**, 719 (2006).
[95]D. de Fontaine, Solid State Phys. **34**, 73 (1979).
[96]O. Delaire, J. Ma, K. Marty, A. F. May, M. A. McGuire, M.-H. Du, D. J. Singh, A. Podlesnyak, G. Ehlers, M. D. Lumsden, and B. C. Sales, Nat. Mater. **10**, 614 (2011).
[97]J. W. Doak, V. Ozoliņš, and C. Wolverton (unpublished).
[98]Incoherent miscibility gap heights have been calculated in DFT for Pb(S,Te), Pb(Te,Se), and Pb(Se,S) previously using a regular-solution model fit to the formation enthalpies of the ordered structure $L1_0$ $[(AC)_1(BC)_1]$ [100] in Table III and Fig. 7].[61,62] However, the authors of Ref. 61 either used an incorrect value for the Boltzmann constant or made an arithmetic error, and the miscibility gap temperatures reported therein are a factor of ∼14 too small. Using their reported regular-solution model parameters

and Eq. (19), we calculate their miscibility gap temperatures to be 2660 K, 1450 K, and 1010 K, for Pb(S,Te), Pb(Te,Se), and Pb(Se,S), respectively. These miscibility gap temperatures are much larger than the temperatures we calculate using a subregular solution model fit to the SQS-16 formation enthalpies. This is due to the fact that the formation enthalpies of $(AC)_1(BC)_1$ [100] ordered structures are much larger than the formation enthalpies of the SQSs (see Table III for our calculated values), and thus $(AC)_1(BC)_1$ [100] is a poor approximation of the random alloy for these systems.

[99] K. Rabe and J. D. Joannopoulos, Phys. Rev. B **36**, 6631 (1987).

[100] E. F. Steigmeier and G. Harbeke, Solid State Commun. **8**, 1275 (1970).

[101] S. Sugai, K. Murase, and H. Kawamura, Solid State Commun. **23**, 127 (1977).

[102] S. Sugai, K. Murase, S. Katayama, S. Takaoka, S. Nishi, and H. Kawamura, Solid State Commun. **24**, 407 (1977).

[103] S. Sugai, K. Murase, T. Tsuchihira, and H. Kawamura, J. Phys. Soc. Jpn. **47**, 539 (1979).

[104] K. A. Abdullin and A. I. Lebedev, Sov. Phys. Solid State **25**, 2055 (1983).

[105] S. Takaoka and K. Murase, Phys. Rev. B **20**, 2823 (1979).

[106] G. S. Pawley, W. Cochran, R. A. Cowley, and G. Dolling, Phys. Rev. Lett. **17**, 753 (1966).

[107] E. S. Božin, C. D. Malliakas, P. Souvatzis, T. Proffen, N. A. Spaldin, M. G. Kanatzidis, and S. J. L. Billinge, Science **330**, 1660 (2010).

[108] Z. Wang and B. Bunker, Phys. Rev. B **46**, 11277 (1992).

[109] B. Dado, Y. Gelbstein, D. Mogilansky, V. Ezersky, and M. P. Dariel, J. Electron. Mater. **39**, 2165 (2009).

[110] A. J. Ardell, R. B. Nicholson, and J. D. Eshelby, Acta Metall. **14**, 1295 (1966).

[111] J. W. Cahn and J. E. Hilliard, J. Chem. Phys. **28**, 258 (1958).

[112] J. W. Cahn, Acta Metall. **10**, 907 (1962).

[113] J. W. Cahn and J. E. Hilliard, J. Chem. Phys. **31**, 688 (1959).

[114] F. Léonard and R. C. Desai, Phys. Rev. B **58**, 8277 (1998).

[115] S. Y. Hu and L. Q. Chen, Acta Mater. **49**, 463 (2001).

[116] S. Y. Hu and L. Q. Chen, Comput. Mater. Sci. **23**, 270 (2002).

[117] F. Léonard and M. Haataja, Appl. Phys. Lett. **86**, 181909 (2005).

[118] S. I. Novikova and N. Kh. Abrikosov, Sov. Phys. Solid State **5**, 1397 (1964).